Journal of Materials Chemistry A

ROYAL SOCIETY OF CHEMISTRY

PAPER

View Article Online
View Journal

Cite this: DOI: 10.1039/d5ta08015k

Porous sulfur-rich polymers from spirobifluorene-derivatives *via* inverse vulcanization for efficient Hg^{2+} capture

Pan Yang,[ab] Xi Deng,[b] Esmé R. Newton-Grain,[b] Frédéric Blanc,[abc] Xiaofeng Wu[b] and Tom Hasell[*ab]

There is a critical need for nanoporous materials for gas storage, molecular separations, and environmental remediation. However, generating porosity directly in as-made inverse vulcanized polymers has remained an unresolved and persistent challenge. Here we report the direct synthesis of porous, sulfur-rich polymers *via* inverse vulcanization in a single-step process that affords high specific surface area (up to 214 $m^2\ g^{-1}$), a hierarchical micro-mesoporous structure, and sulfur content as high as 35 wt%. This is demonstrated by reacting a molecularly rigid and contorted three dimensional monomer (spirobifluorene derivative-2,2′,7,7′-tetraethynyl-9,9′-spirobi[fluorene], TEF) promoting the formation of porosity in an inverse vulcanization process to ensure high sulfur contents. The approach makes the resulting TEF-S polymers highly promising for Hg^{2+} capture in wastewater treatment applications, and they maintain their performance even in the presence of competing ions. As a result, TEF-S highlights the potential of rigid olefinic molecules in designing porous inverse-vulcanized functional materials, paving the way for future innovation in this field.

Received 30th September 2025
Accepted 20th December 2025

DOI: 10.1039/d5ta08015k

rsc.li/materials-a

Introduction

Porous organic materials,[1–3] renowned for their high Brunauer–Emmett–Teller (BET) surface area, are widely employed in adsorption due to their enhanced efficiency. Specific surface area plays a critical role in adsorption, as surface roughness and porosity determine the available binding sites. Among these, functionalized porous frameworks[4–6] have attracted considerable attention for their enhanced performance. In particular, sulfur-containing porous materials, such as covalent organic frameworks[7–9] (COFs) and covalent organic polymers(COPs),[10–16] exhibit a compelling combination of high surface area, tunable pores, and rich chemistry, making them ideal for applications in gas adsorption,[17] catalysis,[18] energy storage,[12] and environmental remediation.[16] Sulfur-containing porous materials are particularly effective in heavy metal adsorption[19–22] due to sulfur's strong affinity for metals like mercury (Hg). Metallic mercury is a toxic environmental pollutant with relatively high solubility in water. It can bioaccumulate through the food chain, leading to high levels of mercury contamination. Since the Minamata Convention[23] on Mercury was adopted in 2013, more than one hundred countries have joined the treaty to collectively reduce anthropogenic mercury emissions and releases, and to protect human health and the environment. As a Lewis base, sulfur can form stable coordination bonds with heavy metal ions, effectively capturing and removing toxic metal pollutants from the environment.

However, despite their promising applications, sulfur-containing porous materials face a major limitation: sulfur is often introduced through post-synthetic modification, which complicates fabrication and limits sulfur content to avoid blocking pores, typically sulfur content is less than 20 wt%.[24,25] Consequently, the adsorption capacity of these materials is restricted, hindering their practical application. Therefore, developing a synthetic strategy that enables the direct incorporation of high sulfur content at the precursor stage is crucial. By designing novel monomers or optimizing synthesis protocols, it becomes possible to obtain polymers with more exposed binding sites capable of forming strong Hg–S coordination, which translates into higher adsorption performance and broadens potential applications. Accordingly, incorporating a high density of accessible sulfur-containing active sites into porous materials is considered a key strategy for enhancing heavy metal adsorption performance.

In recent years, the inverse vulcanization process has garnered significant attention for producing chemically stable and processable polymers with high sulfur content. Inverse vulcanization is a radical copolymerization process in which elemental sulfur undergoes ring-opening at high temperature to generate polysulfide radical chains that then copolymerize

[a]Stephenson Institute for Renewable Energy, University of Liverpool, Liverpool L69 7ZF, UK. E-mail: T.Hasell@liverpool.ac.uk

[b]Department of Chemistry, University of Liverpool, Liverpool L69 7ZD, UK

[c]Leverhulme Research Centre for Functional Materials Design, Materials Innovation Factory, University of Liverpool, Liverpool L69 7ZD, UK

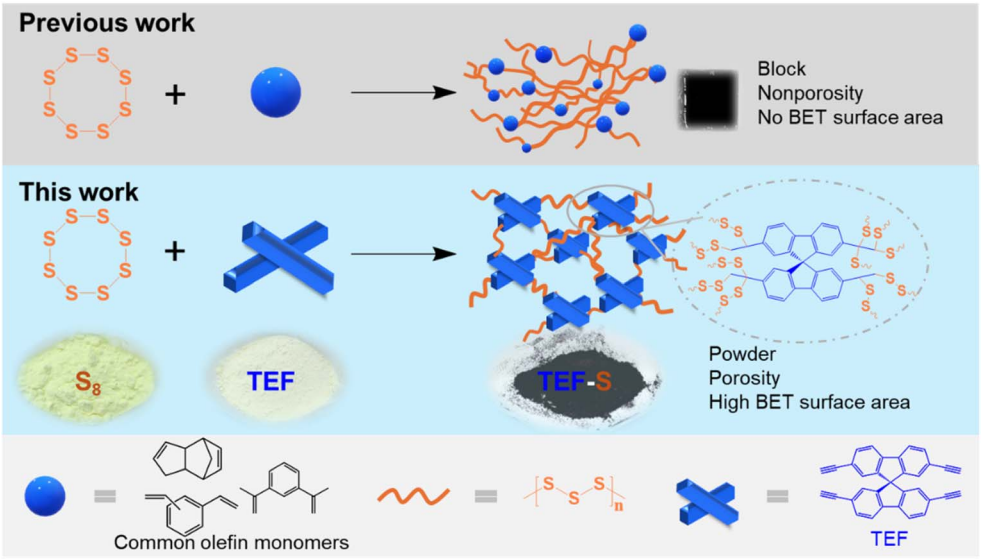

Fig. 1 Schematic comparison of previous work and this study on the synthesis of sulfur-containing porous polymers. Previous methods (top, grey section) involving the direct polymerization of sulfur (S_8) with common olefin monomers result in non-porous, block-like materials with negligible BET surface area. This work (middle, blue section) introduces TEF as a crosslinking monomer, leading to the formation of TEF-S, a porous sulfur-rich polymer with high BET surface area and powder morphology.

with unsaturated organic comonomers, yielding high-sulfur-content polymers. Since 2013, Pyun's pioneering work[26] on inverse vulcanization has inspired extensive research on sulfur-rich polymers, particularly for heavy metal adsorption.[27,28] However, due to the flexibility of S–S bonds, the inherent tendency of long sulfur chains to aggregate limits their application in adsorption processes, resulting in the inability of most sulfur sites to participate in adsorption. Such limitations underscore the importance of chemical or physical modifications of inverse vulcanized polymers. Modifying inverse vulcanized polymers to incorporate porous structures can significantly improve their surface area and porosity, thereby enhancing their mercury adsorption potential. To this end, various post-synthetic strategies have been developed to generate porosity in inverse vulcanized polymers. These approaches include, but are not limited to, the use pore-forming agents,[29–31] carbon dioxide foaming,[32,33] electrospinning,[34,35] carbonization,[36–39] and chemical crosslinking.[40] Although these strategies broaden the material design space, they often suffer from limitations such as complex processing or reduced sulfur content, which hinder their practical applications. Therefore, optimizing preparation protocols is essential for obtaining porous inverse vulcanized polymers and subsequently enhancing their mercury adsorption potential.

Functional building blocks with rigid and non-planar structures are widely employed in the design of porous polymers,[41] as they offer precise control over pore architecture and contribute to unique physical and chemical properties. Among these, spiro[fluorene][42,43] derivatives stand out due to their distinctive spiroconjugation effect,[44,45] ease of synthesis, and high chemical tunability. More importantly, their inherently twisted and three-dimensional (3D) geometry prevents close packing of polymer chains, which promotes the formation of intrinsic free volume and interconnected porous networks. These structural feature makes spiro[fluorene] derivatives particularly well-suited for constructing polymers with high specific surface area and tailored porosity. Building upon these structural features, the integration of spiro[fluorene]-based monomers into inverse vulcanization systems offers a unique opportunity to simultaneously enhance the sulfur content and internal pore structure of the resulting sulfur-rich polymers. In this work (Fig. 1), we present a first example of a porous sulfur-rich polymer directly synthesized through an inverse vulcanization approach. The resulting polymer is achieved using the 3D rigid monomer spirobifluorene-derivative (TEF), which is employed to simultaneously achieve high sulfur content and elevated specific surface area and enhancing the material's adsorption performance for Hg^{2+} capture. The approach opens a new avenue for developing customized porous sulfur-rich materials for applications in adsorption, gas separation, and energy storage.

Results and discussion

To construct high-performance porous sulfur-rich polymers, we designed a tetrafunctional ethynyl monomer-TEF as crosslinker for inverse vulcanization with elemental sulfur (S_8). The strategy enables the formation of a robust, highly cross-linked polymer network through thermal ring-opening polymerization of S_8. The detailed synthesis procedures of TEF are provided in the SI Scheme S1. The structure of the monomer was confirmed by nuclear magnetic resonance (NMR) and mass spectrometry (MS) analysis (Fig. S1–S3). S_8 can undergo ring-opening to form diradicals under heating at 160 °C.[46] Therefore, porous sulfur-rich polymers were synthesized by reacting TEF with S_8 (TEF: S_8 = 50 : 50 wt%) at 160 °C (Fig. 1 and S4). The synthesis of sulfur-free product TEF100-S0-160 was carried out under the same conditions used for the inverse vulcanization

reaction, allowing a direct comparison with the TEF-S polymer prepared under identical conditions. The reaction was monitored by NMR to track the consumption of TEF as it is completely soluble in deuterated chloroform ($CDCl_3$). As shown in Fig. S5, a significant amount of TEF remained in the reaction mixture after 30 minutes of reaction time, but some reddish-brown solid had already formed which was insoluble in $CDCl_3$. Extending the reaction time to 4 hours, only trace TEF was observed in the NMR spectrum. The curing procedure for the polymers is typically conducted at a lower temperature of 140 °C overnight, designed to fully cross-linked network structures. The resulting polymers were designated as TEFX-SY-T, where "X" and "Y" represent the percentage composition of TEF and S respectively and "T" denotes the reaction temperature, where the inclusion of a catalyst was indicated as TEFX-SY-T-Cata.

Characterization of the resulting polymers was performed using a variety of approaches. Fourier transform infrared (FT-IR) data (Fig. 2a) showed the concomitant disappearance of the strong absorption band of ≡C–H asymmetric stretching vibration at 3289 cm^{-1} along with asymmetric stretching vibrations of the –C≡C– peak at 2109 cm^{-1} provides direct spectroscopic evidence for the –C≡C–triple bond consumption during the reaction. The PXRD analysis (Fig. 2b) revealed that both S_8 and TEF exhibited well-defined crystallinity, whereas the resultant polymer TEF50-S50-160 presented lacks Bragg reflections as expected for an amorphous material with no obvious observation of any crystalline domains or residual starting materials. X-ray photoelectron spectroscopy (XPS) and ^{13}C solid-state magic angle spinning (MAS) NMR spectra were obtained to provide strong structural evidence validating the designed polymers. The full XPS energy spectrum (Fig. S6) with only C and S signals indicates that there is strong interaction between TEF and S_8. In the high-resolution XPS spectra of C 1s, the fitted peaks in the C 1s spectrum at 284.8 and 286.2 eV can be ascribed to C–C, C–S, respectively. For the S 2p spectrum (Fig. 2c), there are two peaks at 162.2 and 164.8 eV attributed to S–S and peaks located at 163.8 and 165.3 eV attributed to S–C, respectively. The existence of C–S and S–S bonds signified the formation of sulfur-rich polymers from the S_8 ring after inverse vulcanization. The full description of the ^{13}C MAS NMR spectra of TEF and the polymers spectra is given in the SI supported by spectral assignment (Table S1) and complete set of spectra (Fig. S7–S10). Comparison of these spectra (Fig. 2d) show significant line broadening upon polymerisation, as expected for a distribution of chemical shifts arising from inhomogeneous broadening in amorphous solids. Furthermore, a new resonance at 30 ppm is observed in TEF50-S50-160, which is absent in both the TEF monomer and the TEF100-S0-160 (Table S1). A very substantial reduction in the ^{13}C NMR signals corresponding to alkyne carbons in the 80–85 ppm region is also evident. While these spectra were recorded under standard non-quantitative cross-polarisation (CP) condition, the latter observation nevertheless agrees with the consumption of the TEF alkyne carbons given the similarity of the chemical structures of TEF with the polymers. We note that the FT-IR data point out to

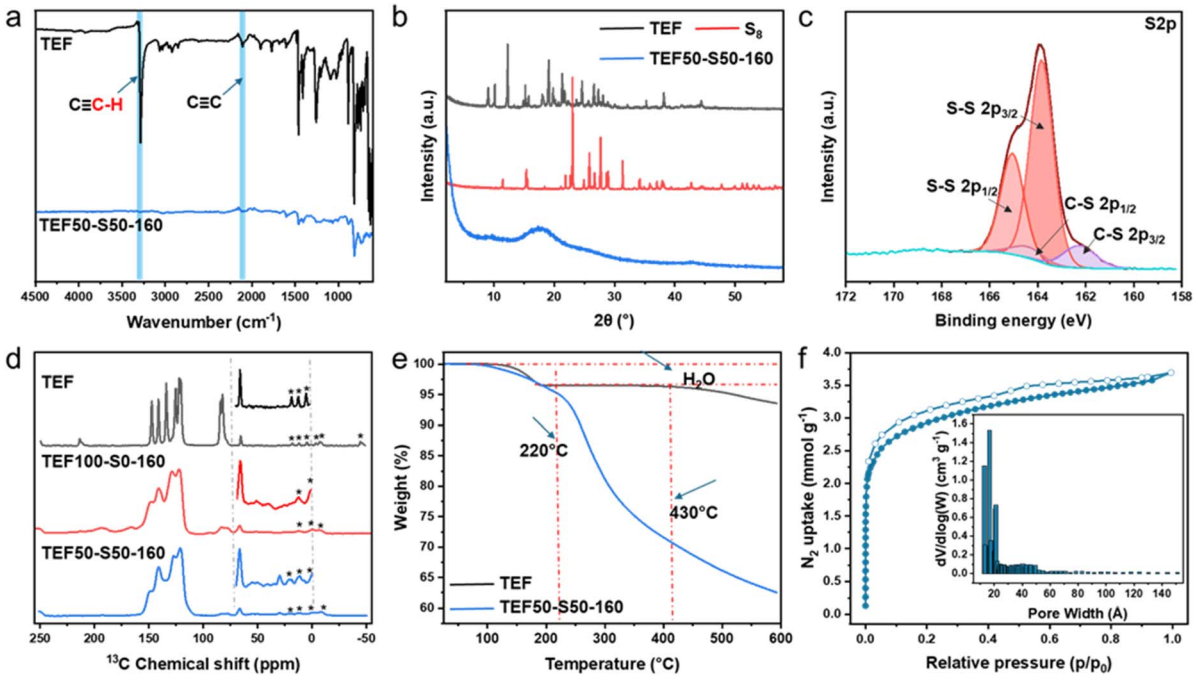

Fig. 2 Characterization of TEF50-S50-160. (a) FT-IR plot about TEF (black) and TEF50-S50-160 (blue). (b) XRD plot of elemental sulfur (red), TEF (black) and polymer TEF50-S50-160 (blue). (c) S 2p XPS spectrum of TEF50-S50-160. (d) ^{13}C cross-polarisation MAS NMR spectra of TEF, TEF100-S0-160 and TEF50-S50-160 with a contact time of 1 ms and spinning at a 13 kHz MAS rate. Inserts show magnified views of the spectra in the 70 to 0 ppm region. Asterisks (*) show the spinning side bands. (e) TGA plot of TEF (black) and TEF50-S50-160 (blue). (f) N_2 sorption isotherms recorded at 77 K about TEF50-S50-160 which showing hysteresis in the desorption isotherm, closed and open symbols represent the adsorption and desorption isotherms, respectively. Insert shows the pore width distribution.

the complete disappearance of the ≡C–H and –C≡C– stretching vibrations and the MAS NMR data may be sensitive to residual TEF trapped in the porous polymers or polymer end chains. An additional ^{13}C MAS NMR spectrum for TEF50-S50-160 recorded under quantitative conditions (Fig. S11) reveal that only less than 2% of residual TEF remains. The 30 ppm peak, which is only present for the TEF50-S50-160 polymer and with a longer contact time of 1 ms supporting the presence of a quaternary carbon, suggests a "–C–CS_2–C" like environment (Fig. 1) based on ^{13}C literature data for C–S moieties typically observed around 20–60 ppm,[47,48] and corroborates the successful incorporation of sulfur into the polymer structure.

The thermal properties of TEF50-S50-160 were analysed by thermogravimetric analysis (TGA) and differential scanning calorimetry (DSC). TGA results (Fig. 2e) revealed that TEF exhibits exceptional thermal stability, with decomposition beginning at a high temperature of 430 °C. TEF50-S50-160 also exhibits great thermal stability, does not show significant mass loss before 200 °C, which is comparable to other reported inverse vulcanized polymers.[26] DSC analysis shows the absence of a discernible glass transition temperature (T_g) for the resultant polymers. The result could be attributed to the rigid carbon backbone structure of TEF and high degree of crosslinking. DSC also proved there is no crystalline elemental sulfur remaining in polymer TEF50-S50-160 (Fig. S12). The surface morphology of the polymer was characterized using SEM. As shown in the Fig. S13, the polymer surface displays distinct pore channels and a rough, uneven texture (Fig. S13a and b). This is in stark contrast to the smooth and flat surface of the TEF100-S0-160 (Fig. S13c and d).

The rigid, and sterically hindered architecture of TEF suggested inherent potential for porosity generation in the resulting polymer. To test this hypothesis, the permanent porosity of TEF50-S50-160 was evaluated using N_2 adsorption–desorption isotherms at 77 K (Fig. S14). At 77 K, TEF50-S50-160 demonstrated a BET specific surface area of 126 $m^2\ g^{-1}$. The adsorption isotherm showed features typical of microporous materials, characterized by a type I adsorption isotherm. Noteworthy, the BET surface area of this material is markedly higher than that of comparable materials, indicating its superior surface accessibility and porosity.[35,49] The BET surface area of the TEF100-S0-160 obtained under comparable reaction conditions is only 5 $m^2\ g^{-1}$ (Fig. S15). Such a result could be attributed to the fact that the inverse vulcanization between alkyne and sulfur groups occurs more readily than the homocoupling of terminal alkynes themselves. In addition, the rigid TEF molecule can reduce the intermolecular interaction forces, thereby mitigate polymer chain contractions and facilitating the formation of a slightly loosely packed porous network under the current experimental conditions.

It has been evidenced that the physicochemical properties of the resulting polymers exhibit pronounced dependence on synthetic conditions. Critical parameters including curing duration, reaction temperature, monomer feed ratio, and catalyst presence/absence were systematically investigated, evaluating their respective impacts on the polymer's BET surface area. Firstly, the effect of curing time was investigated. Based on the results of the time-monitoring experiments, the reaction duration was set to 4 hours, with curing times selected as 12 hours, 24 hours, and 48 hours at 140 °C. As the curing time was extended, a significant increase in the BET specific surface area was observed. Specifically, the BET specific surface area at 12 h, 24 h, and 48 h are 121 $m^2\ g^{-1}$ (Fig. S14), 146 $m^2\ g^{-1}$ (Fig. S16), and 214 $m^2\ g^{-1}$ (Fig. 2f), respectively. The XRD pattern (Fig. S17) confirms the absence of free crystalline sulfur in these polymers. The higher BET surface area with prolonged curing time may be due to the reconstruction of the reversible S–S bonds in the slight-loosely packed porous matrix of the polymer. The FT-IR and TGA spectra are presented in Fig. S18 and S19, revealing a fully completed polymerization. Additionally, elemental analysis (Fig. S20 and Tables S2–S3) indicates that extending the curing time does not necessarily increase the sulfur content of the resulting polymer. Next, the curing time was fixed at 12 hours, and the initial reaction temperature was increased to 180 °C to study the effect of temperature. However, no significant improvement in the BET specific surface area was observed; instead, a relatively low value of 79 $m^2\ g^{-1}$ was obtained (Fig. S21). Such a result may be attributed to that, on one hand, the terminal alkynes are prone to oxidation at elevated temperatures, reducing the number of functional groups available for the inverse vulcanization reaction; on the other hand, higher temperatures can promote the sulfur volatilization, leading to depletion of sulfur content within the reaction system. Catalysts play a crucial role in the study of inverse vulcanized polymers, as they not only help reduce the reaction temperature but also enable use of monomers that are difficult to react with sulfur.[50–52] We also investigated the effect of catalyst on the BET specific surface area of sulfur-rich polymers at different temperatures. With the assistance of the catalyst, the reaction temperature for inverse vulcanized polymers can be reduced to 140 °C or even lower. It can be observed that, with the introduction of the Zn based catalyst (see SI), the BET specific surface area increases as the temperature rises (see Fig. S22–S24). A higher BET surface area, of 176 $m^2\ g^{-1}$, was achieved at a temperature of 180 °C (TEF50-S50-180-Cata, Fig. S24), comparing to TEF50-S50-140-Cata (25 $m^2\ g^{-1}$) and TEF50-S50-160-Cata (34 $m^2\ g^{-1}$). However, the increase in BET specific surface area is accompanied by a decrease in sulfur content. At a temperature of 160 °C, the BET specific surface area reached 33 $m^2\ g^{-1}$ (TEF50-S50-160-Cata, Fig. S23), with the sulfur content in the polymer peaking at 35.58%. Conversely, when the polymer displayed a higher BET specific surface area (TEF50-S50-180-Cata, 176 $m^2\ g^{-1}$), the sulfur content decreased to 28.64% (see Table S4). This is most likely attributed to increased chain flexibility resulting from higher sulfur content, which leads to a reduction in BET surface area. Further investigation was conducted to explore the effect of varying the monomer feed ratio on the BET specific surface area. The results indicate that as the sulfur content in the feed ratio increases, the BET specific surface area decreases, which is accompanied by an increase in the sulfur content of the polymer (see Fig. S25–S29). At a 50 : 50 feed ratio, the polymer maintains a relatively high BET specific surface area while also exhibiting a high sulfur content of 27%. The basic

characterization of the porous polymer TEF-S (FT-IR, DSC, TGA, XRD) is provided in Fig. S30–S33, which is consistent with the data of TEF50-S50-160.

It is remarkable that porous sulfur-rich polymers in this work can be directly synthesized through the polymerization of monomers with sulfur. These polymers possess high sulfur content and a certain BET specific surface area, which led us to explore their affinity for small gas sorption (CO_2, H_2 and CH_4). TEF50-S50-160 (curing 48 hours), which has the highest BET surface area among these porous polymers, was chosen for testing. The CO_2 adsorption performance of the polymers was investigated at 273 K and 298 K (Fig. S34). It was observed that with increasing pressure, the amount of adsorbed CO_2 also increased. At 1 bar and 273 K, the adsorption capacity reached 2 mmol g^{-1}. The adsorption performance of TEF50-S50-160 was comparable to previously reported sulfur-containing microporous polymers[53,54] and carbonized inverse vulcanized polymers.[36] The hydrogen (H_2) adsorption behaviour of the material was also tested at 77 K, with the results shown in Fig. S35. At 77 K, the material exhibited an H_2 adsorption capacity of 3 mmol g^{-1}, surpassing previously reported inverse vulcanized polymers[36] used for H_2 adsorption with post-synthesis methods. The enhanced H_2 adsorption capacity can be attributed to relatively weak van der Waals interactions, where hydrogen molecules are physically adsorbed onto the material's high surface area. We also evaluated the CH_4 adsorption performance of the porous material, with corresponding data presented in SI (Fig. S36). Achieving such promising results through a single-step synthesis method represents a significant advancement.

Porous organic polymers with high sulfur content are highly attractive in the field of wastewater treatment. Before performing the Hg^{2+} adsorption measurements, the stability of the material after deionized water treatment was systematically evaluated. As shown in Fig. S37 and S38, the BET and TGA results demonstrate that the polymer maintains both its porous structure and thermal stability after 24 h of water treatment, indicating excellent hydrolytic stability with no significant structural collapse. TEF-sulfur copolymers were employed for the removal of Hg^{2+} from water. Elemental sulfur was used as a control group for comparison with the TEF-sulfur copolymers. The adsorption capacity of the obtained polymers for mercury was tested under identical conditions, and the results are presented in Fig. S39. Elemental sulfur was only able to remove trace amounts of metal ions from water, with an adsorption capacity of 0.6 mg g^{-1}. In contrast, the obtained porous sulfur-rich polymers demonstrated a significantly enhanced capacity for removing mercury ions from water, with adsorption capacities generally exceeding 35 mg g^{-1}. Among them, TEF50-S50-180-Cata, which possessed the higher specific surface area and much high sulfur content, exhibited the best adsorption capacity, reaching 79 mg g^{-1}. We found that achieving relatively good adsorption performance requires a combination of high specific surface area and relatively high sulfur content. In this context, sulfur serves as the active adsorption site, while a hierarchical porous structure with high specific surface area facilitates efficient diffusion, provides pore connectivity, and maximizes the number of exposed active sites. The accessible sulfur is beneficial for adsorption applications. Therefore, a compromise must be made between increasing the sulfur content to provide more adsorption sites and avoiding excessive sulfur loading that would reduce the porosity. Given that the sulfur-free product TEF100-S0-160 exhibits negligible Hg^{2+} adsorption, the small fraction of residual monomer (<2%) should have minimal impact on the Hg^{2+} uptake capacity of the material. Meanwhile, the SEM, XRD, XPS and TGA of the material after metal adsorption are shown in Fig. S40–S45. In addition, the material also exhibits appreciable stability under the Hg^{2+} adsorption conditions. The data confirm the successful adsorption of Hg^{2+}.

The samples with the highest specific surface area (TEF50-S50-160) and the highest sulfur content (TEF50-S50-160-Cata) were selected to describe the sorption process for $HgCl_2$ (Fig. S46–S47 and Tables S5–S11). These samples were used to investigate the adsorption behavior and evaluate their capacity to remove $HgCl_2$ from aqueous solutions under controlled conditions. Meanwhile, we synthesized a sulfur-dicyclopentadiene (S-DCPD) polymer and used a commercially available activated carbon as a control. S-DCPD is a typical high-

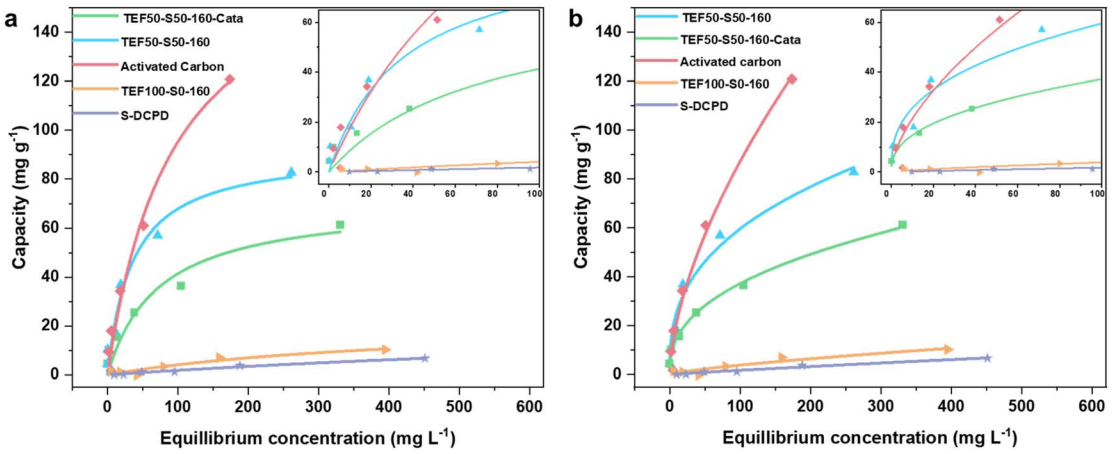

Fig. 3 (a) Non-linear fitting of the Langmuir isotherm model for $HgCl_2$ sorption. (b) Non-linear fitting of Freundlich isotherm model for $HgCl_2$ sorption. Model parameters are listed in Tables S6–S8. Experimental measurements shown as symbols, with fittings as lines.

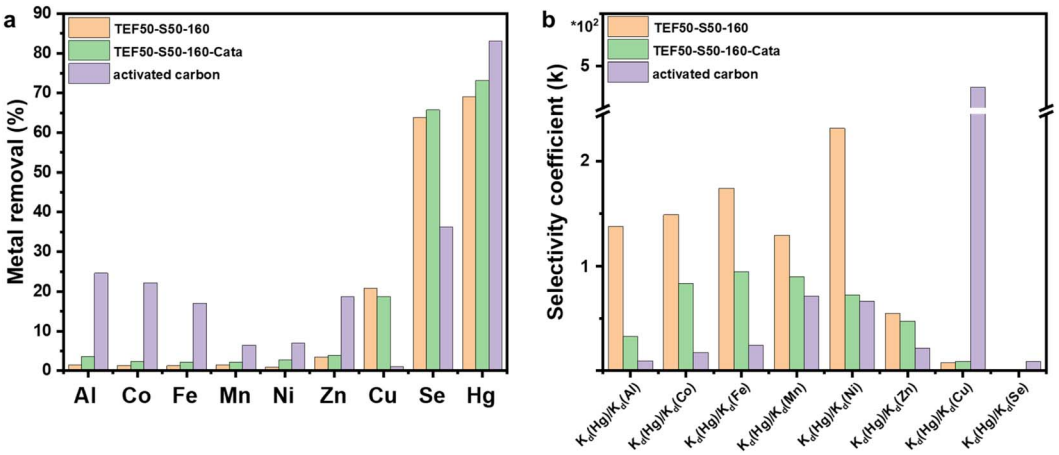

Fig. 4 Comparison of (a) metal removal efficiency and (b) selectivity coefficients (k) data for three different materials, with activated carbon serving as the control. The bar chart illustrates the selective adsorption capacities of different materials in the same trace metal solution. TEF-S porous materials, characterized by a high BET surface area, demonstrated good selectivity for Hg and Se. Parameters are listed in Tables S12–S14.

sulfur-content inverse vulcanized polymer. However, the high flexibility of sulfur chains can lead to the dense packing of molecular chains as the sulfur content increases, resulting in a non-porous structure in sulfur-rich polymer materials. As shown in Fig. 3, S-DCPD exhibited negligible mercury adsorption capacity under the same testing conditions, with a maximum adsorption capacity of only 6.27 mg g^{-1}. Both TEF50-S50-160 and TEF50-S50-160-Cata demonstrate excellent adsorption performance for Hg^{2+}, especially at the low concentrations which are industrially relevant. The performance makes these new materials comparable to commercially available activated carbon in terms of capacity, which only outperformed the TEF50-S50-160 at high concentrations, despite the activated carbon having over four times the surface area. In practical wastewater treatment applications, the adsorption of low concentrations of mercury is of particular significance. Activated carbon adsorbs metallic mercury through a simple physical adsorption process, which can easily lead to mercury leaching and secondary contamination during subsequent treatment processes. In contrast, the inverse vulcanized polymers we obtained utilize sulfur as a Lewis base, which can form coordination complexes with mercury ions. The interaction is stronger than the physical adsorption of activated carbon, making it a safer option for mercury removal while achieving similar adsorption performance.

In real-world applications, mercury ion concentrations are typically below 1 ppm, and there are also competing ions present. Therefore, we tested the ability of the obtained polymers to selectively adsorb metallic mercury in simulated contaminated water, which contains various metals such as Co^{2+}, Zn^{2+}, and others. Experimental results showed that (Fig. 4a), among the numerous pollutant ions, the porous polymers exhibited high selectivity for Hg^{2+} and Se. The polymers were able to remove over 70% of mercury and more than 65% of selenium from the simulated wastewater, even when the mercury concentration was extremely low (even at ppb level). The selectivity coefficient (k) is a key parameter to evaluate the Hg^{2+} adsorption selectivity of a porous adsorbent in the presence of competing ions. As shown in Table S13 and Fig. 4b, the TEF50-S50-160 and TEF50-S50-160-Cata materials exhibit significantly higher selectivity for mercury (Hg) compared to activated carbon in the presence of competing metal ions such as Al, Co, Fe, Mn, Ni, and Zn. Notably, TEF50-S50-160 achieves a selectivity coefficient of 154 for Hg in comparison to Al, whereas activated carbon demonstrates a considerably lower value of only 14.99, highlighting the superior affinity of TEF50-S50-160 for Hg. At this point, activated carbon, on the other hand, shows significantly lower selectivity coefficient for mercury ions in the presence of competing ions. The high selectivity of TEF-S for Hg^{2+} can be attributed to the strong Lewis base character of sulfur, which forms stable coordination complexes with mercury ions. This interaction is stronger than the physical adsorption observed in activated carbon, leading to higher selectivity even in the presence of competing ions such as Co^{2+} and Zn^{2+}. This experiment demonstrates that, even in the presence of competing ions, the TEF50-S50 porous polymer still exhibits a high selective adsorption capacity for mercury ions.

Conclusions

This work reports the direct synthesis of porous sulfur-rich polymers *via* a one-step inverse vulcanization process using a rigid and contorted three-dimensional spirobifluorene-derivative (TEF) – and elemental sulfur. The resulting polymers exhibit hierarchical micro-mesoporous structures, with a BET specific surface area reaching up to 214 m^2 g^{-1} and a high sulfur content. To the best of our knowledge, this approach represents the first example of directly synthesized porous sulfur-rich polymers obtained *via* inverse vulcanization. Furthermore, the polymers show strong affinity for both CO_2 and H_2, suggesting promising potential for molecular separation applications arising from their microporosity and high heteroatom content. Owing to their intrinsic porosity and high sulfur content, TEF–S polymers are also well suited for wastewater treatment applications, demonstrating high efficiency in the removal of mercury ions even at low concentrations, while

maintaining their performance in the presence of competing ions.

The porous structure of these materials significantly increases their specific surface area, providing abundant active sites for metal ions and gas molecule adsorption and transport. Furthermore, the incorporation of heteroatoms, particularly sulfur, effectively modifies the surface chemistry of the material, enhancing gas adsorption performance. Porous inverse vulcanized polymers not only exhibit excellent adsorption capabilities but also possess advantages such as low sulfur cost, abundant feedstock sources, and simple fabrication processes. Combined with their high surface area and sulfur-rich composition, these attributes make them highly promising materials for applications including wastewater treatment, gas separation, energy storage, and lithium-sulfur batteries. Looking ahead, further optimization of their properties through rational molecular design and precise structural tuning is expected to unlock new opportunities, providing valuable insights and technological support for applications in environmental remediation, catalysis, and advanced energy systems.

Author contributions

T. H., X. F. W. and P. Y. conceived the project. P.Y. carried out the experimental works. P. Y. T. H. and X. F. W. performed the characterizations. E. R. N.-G. and F. B. carried out the solid-state NMR. P. Y. and X. D. carried out mercury adsorption and performed the characterizations. T. H. X. F. W. and F. B. thoroughly revised the manuscript. All authors interpreted the data and contributed to the preparation of the manuscript.

Conflicts of interest

There are no conflicts to declare.

Data availability

The data supporting this article have been included as part of the Supplementary information (SI). Supplementary information: all experimental procedures, additional FT-IR, NMR, MAS NMR XPS spectra, BET, DSC, SEM, TGA, XRD data, EDX maps, CHNS contents, gas sorption isotherms, and mercury capture and adsorption data. See DOI: https://doi.org/10.1039/d5ta08015k

Acknowledgements

P. Y. thanks the China Scholarship Council (CSC) for awarding her scholarship. P. Y. thanks the Materials Innovation Factory (MIF) team members for their support in operating instruments. E. R. N.-G. thanks the University of Liverpool for a PhD studentship. T. H. is supported by a Royal Society University Research Fellowship.

Notes and references

1 S. Das, P. Heasman, T. Ben and S. Qiu, *Chem. Rev.*, 2017, **117**, 1515–1563.
2 D. H. Yang, Y. Tao, X. Ding and B. H. Han, *Chem. Soc. Rev.*, 2022, **51**, 761–791.
3 A. G. Slater and A. I. Cooper, *Science*, 2015, **348**, aaa8075.
4 A. Modak, P. Bhanja, M. Selvaraj and A. Bhaumik, *Environ. Sci.: Nano*, 2020, **7**, 2887–2923.
5 A. Stein, Z. Wang and M. A. Fierke, *Adv. Mater.*, 2009, **21**, 265–293.
6 J. Landers, G. Y. Gor and A. V. Neimark, *Colloids Surf., A*, 2013, **437**, 3–32.
7 D. G. Wang, N. Li, Y. Hu, S. Wan, M. Song, G. Yu, Y. Jin, W. Wei, K. Han, G. C. Kuang and W. Zhang, *ACS Appl. Mater. Interfaces*, 2018, **10**, 42233–42240.
8 J. M. Chen, H. Duan, Y. Kong, B. Tian, G. H. Ning and D. Li, *Energy Fuels*, 2022, **36**, 5998–6004.
9 Q. Jiang, Y. Li, X. Zhao, P. Xiong, X. Yu, Y. Xu and L. Chen, *J. Mater. Chem. A*, 2018, **6**, 17977–17981.
10 M. B. Preefer, B. Oschmann, C. J. Hawker, R. Seshadri and F. Wudl, *Angew. Chem., Int. Ed.*, 2017, **56**, 15118–15122.
11 R. Zou, W. Liu and F. Ran, *InfoMat*, 2022, **4**, e12319.
12 Y. Fu, W. Yu, W. Zhang, Q. Huang, J. Yan, C. Pan and G. Yu, *Polym. Chem.*, 2018, **9**, 4125–4131.
13 W. Kiciński, M. Szala and M. Bystrzejewski, *Carbon*, 2014, **68**, 1–32.
14 J. Li, S. Wang, X. Cao, H. Huang and D. Cao, *Mater. Chem. Front.*, 2021, **5**, 3428–3435.
15 B. Zheng, X. Lin, X. Zhang, D. Wu and K. Matyjaszewski, *Adv. Funct. Mater.*, 2020, **30**, 1907006.
16 L. Huang, R. Liu, J. Yang, Q. Shuai, B. Yuliarto, Y. V. Kaneti and Y. Yamauchi, *Chem. Eng. J.*, 2021, **408**, 127991.
17 C. Liu, Y. Zhi, Q. Yu, L. Tian, M. Demir, S. G. Colak, A. A. Farghaly, L. Wang and X. Hu, *ACS Appl. Nano Mater.*, 2024, **7**, 5434–5441.
18 Y. Zhang and S. N. Riduan, *Chem. Soc. Rev.*, 2012, **41**, 2083–2094.
19 H. Shin, J. Kim, D. Kim, V. H. Nguyen, S. Lee, S. Han, J. Lim and K. Char, *J. Mater. Chem. A*, 2018, **6**, 23542–23549.
20 S. Y. Chen, J. Q. Wu and S. Sung, *J. Hazard. Mater.*, 2022, **424**, 127257.
21 D. Ko, J. S. Lee, H. A. Patel, M. H. Jakobsen, Y. Hwang, C. T. Yavuz, H. C. B. Hansen and H. R. Andersen, *J. Hazard. Mater.*, 2017, **332**, 140–148.
22 H. Tian, J. Guo, Z. Pang, M. Hu and J. He, *Nanoscale*, 2020, **12**, 16543–16555.
23 R. Kessler, *Environ. Health Perspect.*, 2013, **121**, A304.
24 L. Yang, Z. Zhan, L. Zhao, C. Zhang, S. Wang, W. Hu and G. Zhu, *Chem. Sci.*, 2025, **16**, 775–783.
25 T. Liu, J.-X. Che, Y.-Z. Hu, X.-W. Dong, X.-Y. Liu and C.-M. Che, *Chem.–Eur. J.*, 2014, **20**, 14090–14095.
26 W. J. Chung, J. J. Griebel, E. T. Kim, H. Yoon, A. G. Simmonds, H. J. Ji, P. T. Dirlam, R. S. Glass, J. J. Wie, N. A. Nguyen, B. W. Guralnick, J. Park, Á. Somogyi,

P. Theato, M. E. Mackay, Y.-E. Sung, K. Char and J. Pyun, *Nat. Chem.*, 2013, **5**, 518–524.
27 F. G. Müller, L. S. Lisboa and J. M. Chalker, *Adv. Sustainable Syst.*, 2023, **7**, 2300010.
28 A. P. Grimm, J. M. Scheiger, P. W. Roesky and P. Théato, *Polym. Chem.*, 2022, **13**, 5852–5860.
29 M. J. Worthington, R. L. Kucera, I. S. Albuquerque, C. T. Gibson, A. Sibley, A. D. Slattery, J. A. Campbell, S. F. Alboaiji, K. A. Muller and J. Young, *Chem.–Eur. J.*, 2017, **23**, 16219–16230.
30 M. Arslan, B. Kiskan and Y. Yagci, *Macromolecules*, 2016, **49**, 767–773.
31 A. M. Abraham, S. V. Kumar and S. M. Alhassan, *Chem. Eng. J.*, 2018, **332**, 1–7.
32 H. K. Lin, Y. S. Lai and Y. L. Liu, *ACS Sustain. Chem. Eng.*, 2019, **7**, 4515–4522.
33 T. Hasell, D. Parker, H. Jones, T. McAllister and S. Howdle, *Chem. Commun.*, 2016, **52**, 5383–5386.
34 M. W. Thielke, L. A. Bultema, D. D. Brauer, B. Richter, M. Fischer and P. Theato, *Polymers*, 2016, **8**, 266.
35 L. A. Limjuco, G. M. Nisola, K. J. Parohinog, K. N. G. Valdehuesa, S.-P. Lee, H. Kim and W.-J. Chung, *Chem. Eng. J.*, 2019, **378**, 122216.
36 J. C. Bear, J. D. McGettrick, I. P. Parkin, C. W. Dunnill and T. Hasell, *Microporous Mesoporous Mater.*, 2016, **232**, 189–195.
37 M. Mann, X. Luo, A. D. Tikoalu, C. T. Gibson, Y. Yin, R. Al-Attabi, G. G. Andersson, C. L. Raston, L. C. Henderson and A. Pring, *Chem. Commun.*, 2021, **57**, 6296–6299.
38 R. Shamsuddin, A. S. M. Ghumman, R. Steven, A. Sami, S. Waqas and Z. N. Ahmad, *ACS ES&T Water*, 2025, **5**, 1499–1509.
39 J. S. M. Lee, D. J. Parker, A. I. Cooper and T. Hasell, *J. Mater. Chem. A*, 2017, **5**, 18603–18609.
40 S. Petcher, B. Zhang and T. Hasell, *Chem. Commun.*, 2021, **57**, 5059–5062.
41 L. Tan and B. Tan, *Chem. Soc. Rev.*, 2017, **46**, 3322–3356.
42 N. B. McKeown and P. M. Budd, *Macromolecules*, 2010, **43**, 5163–5176.
43 H. E. Simmons and T. Fukunaga, *J. Am. Chem. Soc.*, 1967, **89**, 5208–5215.
44 J. Salbeck, *Ber. Bunsenges. Phys. Chem.*, 1996, **100**, 1667–1677.
45 N. Johansson, D. Dos Santos, S. Guo, J. Cornil, M. Fahlman, J. Salbeck, H. Schenk, H. Arwin, J. Brédas and W. Salanek, *J. Chem. Phys.*, 1997, **107**, 2542–2549.
46 B. Meyer, *Chem. Rev.*, 1976, **76**, 367–388.
47 V. K. Shankarayya Wadi, K. K. Jena, S. Z. Khawaja, K. Yannakopoulou, M. Fardis, G. Mitrikas, M. Karagianni, G. Papavassiliou and S. M. Alhassan, *ACS Omega*, 2018, **3**, 3330–3339.
48 K. Kuwabara, F. Horii and Y. Ogawa, *J. Mol. Struct.*, 2002, **602**, 79–87.
49 S. Lyu, Z. Z. Abidin, T. C. S. Yaw and M. F. M. G. Resul, *Environ. Sci. Pollut. Res.*, 2024, **31**, 29264–29279.
50 X. Wu, J. A. Smith, S. Petcher, B. Zhang, D. J. Parker, J. M. Griffin and T. Hasell, *Nat. Commun.*, 2019, **10**, 647.
51 J. H. Hwang, J. M. Lee, J. H. Seo, G. Y. Noh, W. Byun, S. Kim, W. Lee, S. Park, D.-G. Kim and Y. S. Kim, *Green Chem.*, 2023, **25**, 4641–4646.
52 L. J. Dodd, Ö. Omar, X. Wu and T. Hasell, *ACS Catal.*, 2021, **11**, 4441–4455.
53 S. H. Je, O. Buyukcakir, D. Kim and A. Coskun, *Chem*, 2016, **1**, 482–493.
54 G. Kupgan, L. J. Abbott, K. E. Hart and C. M. Colina, *Chem. Rev.*, 2018, **118**, 5488–5538.

